



Hierarchical Nested Cascade Control Framework for Enhanced Energy Management in Fuel Cell Hybrid Electric Vehicles

Peyman Bayat^{1*}, Pezhman Bayat²

^{1,2}Department of Electrical Engineering, Hamedan University of Technology, Hamedan, Iran

ARTICLE INFO

Article history:

Received : 23 Mar 2025

Accepted: 30 Aug 2025

Published: 29 Sep 2025

Keywords:

Adaptive proportional–integral controller

Backstepping controller

Energy management system

Fuel cell hybrid electric vehicles (FCHEVs)

Hierarchical nested cascade control

ABSTRACT

This study proposes a hierarchical nested cascade control framework to enhance voltage regulation and current management in fuel cell hybrid electric vehicles (FCHEVs). The architecture addresses limitations of conventional cascade control by reducing design complexity and improving resilience under dynamic and uncertain conditions. It integrates three coordinated layers: an outer control level (OCL) employing an adaptive proportional–integral controller for DC bus voltage regulation, and two internal layers, middle (MCL) and inner (ICL), implemented via backstepping controllers for precise current control of fuel cells, batteries, and supercapacitors. By combining nonlinear control with model reference adaptive control, the system dynamically tunes parameters to maintain voltage stability across variable load profiles. Simulations using the WLTC-Class 3 cycle show that the proposed strategy (Case 1) achieves superior battery sustainability, with a final SOC of 74.2%, compared to 71% and 72.5% in benchmark strategies (Cases 2 and 3). Under battery aging (20% increased resistance, 15% reduced capacity), DC bus voltage remains within ± 3.5 V of the 380 V reference, with only 18% ripple increase and 0.8% additional SOC depletion. A resilience index of 96.5% confirms robustness, outperforming benchmarks (84.2%, 89.7%). To further validate performance under real-world urban conditions, date-specific driving cycles tailored for Shiraz city were employed. Results confirm the framework's effectiveness in sustaining stability, efficiency, and scalability for next-generation FCHEV energy systems.

1. Introduction

Conventional internal combustion engine vehicles, primarily reliant on fossil fuels, are major contributors to greenhouse gas emissions and urban air pollution; transitioning to clean and energy-efficient electric vehicles (EVs) offers a technically feasible and environmentally responsible solution, in line with international decarbonization strategies aimed at mitigating climate change [1]. In EV applications, energy demand exhibits significant variability, influenced by both driving conditions and driver behavior.

Typically, a sole primary energy source lacks the responsiveness required to manage rapid fluctuations in demand, which can accelerate system degradation and reduce operational lifespan; consequently, multi-source energy systems are often employed to enhance reliability and dynamic performance.

Among the various energy sources gaining increased attention, proton exchange membrane fuel cells (PEMFCs) have emerged as a focal point due to their high efficiency, environmental benefits, and suitability for transportation

*Corresponding Author: Peyman Bayat
Email Address: peyman.bayat@hut.ac.ir
<https://doi.org/10.22068/ase.2025.722>

applications. PEMFCs offer a clean alternative by converting chemical energy into electricity through an electrochemical process, generating only water and heat as byproducts [2]. These features position them as promising candidates for addressing the energy and environmental challenges associated with transportation. Fuel cell electric vehicles (FCEVs) are particularly notable for their extended driving range, short refueling times, silent operation, and zero local emissions [3]. As a result, interest in FCEVs is on the rise among researchers. However, FCEVs also face technical hurdles such as slow transient response and inability to recuperate braking energy. To address these limitations, integrating energy storage systems (ESS) such as batteries and supercapacitors (SC) through hybridization has emerged as a practical approach [4].

SCs demonstrate remarkable energy storage properties, including rapid charge and discharge capability, extended lifecycle, and stable performance across diverse temperature ranges, rendering them well-suited for high-power and repetitive cycling applications. Conversely, lithium-ion batteries are distinguished by their fast response times, low self-discharge rates, long cycle life, and high energy density. Moreover, implementing an appropriate liquid cooling system remains a key challenge, as it plays a crucial role in ensuring uniform temperature distribution and effective heat dissipation [5].

These ESSs are frequently integrated into hybrid configurations to address the limitations associated with standalone FCEVs. When paired these ESS with PEMFCs, the resulting configuration is referred to as a fuel cell hybrid electric vehicle (FCHEV). In multi-source energy systems, optimal allocation of power across various sources must be managed based on their dynamic response characteristics. Hence, given the distinct operating characteristics of PEMFCs and ESSs, an energy management strategy (EMS) is critical for optimal power distribution. Various EMSs are designed based on system-specific goals, each carrying its own merits and limitations. The study outlined in [6] centers on the creation of a simulation model for a FCHEV traction system, developed using the MATLAB Simulink environment. The research investigates various topological configurations of battery systems and hybrid traction architectures. The proposed model employs a PEMFC as the principal energy source. To accommodate the irregularities in transport load demand, a high-performance buffer storage unit based on lithium-

titanium-oxide battery technology is integrated into the system design.

Recent studies have placed growing emphasis on the development of EMS, with a particular focus on heuristic rule-based approaches that do not involve optimization techniques [7, 8]. These systems function in real-time without predictive driving data but depend on predefined logic rules based on battery state of charge (SOC) and load requirements. Although simple to implement, these approaches are reliant on designer expertise and offer limited optimization [9]. Optimization-based EMSs are typically classified into global and instantaneous methods. Instantaneous schemes, such as the equivalent consumption minimization strategy, can operate without prior data, demand fewer computational resources, and support real-time power management [10]. Conversely, global methods, like dynamic programming (DP), require complete knowledge of driving profiles, which is impractical due to inherent unpredictability in real-world vehicle operation. Thus, globally optimized EMSs are mostly used as reference models for performance evaluation [11]. Article [12] introduced a dynamic rule-based control approach that adapts to load conditions and integrates an optimal control scheme derived through DP, enabling efficient real-time energy management. Despite effectiveness of DP, the dynamic rule-based control strategy presents certain limitations. The reliance on predefined rules may constrain adaptability under highly unpredictable load variations or novel operational scenarios. Furthermore, while dynamic programming offers optimal control capabilities, its computational complexity can hinder real-time implementation, particularly in systems with high dimensionality or constrained processing resources.

Article [13] developed a reinforcement learning framework tailored for FCHEVs equipped with batteries and SCs. The system employs a fuzzy filtering mechanism to layer the SC power signals, while the equivalent consumption minimization strategy algorithm strikes a balance between holistic learning processes and real-time applicability. This approach enhances computational efficiency, suppresses fluctuations in fuel cell (FC) output, and improves fuel economy. While this approach provides a balance between global learning and real-time application, it might not always guarantee optimality under rapidly changing driving conditions.

Another core challenge lies in dynamically optimizing PEMFC output, as multi-physical systems whose performance fluctuates with

operational conditions [14]. The optimal output power point, such as the highest efficiency operating level, continually shifts within the system's working space. Operating PEMFCs within high-efficiency zones not only conserves energy but also prolongs lifespan [15]. Real-time adaptation of FC parameters is therefore necessary, which can be achieved via online identification techniques such as recursive least squares or the extended Kalman filter algorithm [16]. A key shortcoming of this approach lies in its limited capacity for real-time adaptation of FC parameters, which are highly sensitive to operational conditions.

In a novel and inventive approach, [17] proposed an integral backstepping control method in conjunction with a rule-based EMS for battery–SC hybrid EVs. However, relying exclusively on rule-based management is often suboptimal [18], particularly due to the nature of power allocation among the vehicle's energy sources, which includes both low and high-frequency components. When batteries are subjected to high-frequency power demands, their operational lifespan may be compromised, leading to accelerated degradation. Moreover, while the backstepping approach offers indirect regulation of the DC-bus voltage, it adds considerable complexity to both the controller's architecture and functional dynamics. This stems from the need to develop dedicated virtual controllers for each system state variable, which fosters intricate interactions between the virtual controllers and their physical counterparts. Such complexities may trigger unexpected oscillations or instability under specific operating scenarios, most notably during mode transitions between propulsion and regenerative braking phases [18].

Recent studies have underscored the critical need for multidimensional failure modeling in lithium-ion battery packs deployed in electric vehicles, especially under demanding operational stress conditions. Within this framework, the fuzzy logic-based failure mode and effects analysis method proposed in [19] provides meaningful insights into key failure contributors, including sealing integrity, battery management system performance, thermal regulation efficiency, and mechanical assembly robustness. These findings collectively reinforce the imperative of embedding fault-tolerant strategies into control architectures to enhance system reliability, safety, and longevity. Such integration not only mitigates potential risks but also ensures sustained performance across diverse operating environments and evolving vehicular demands.

In Article [20], a new hybrid cascade control framework combining proportional–integral (PI) and backstepping methods was introduced to manage DC-bus voltage in the presence of uncertainties and fluctuating loads, while also handling current reference tracking for the onboard energy sources. Although this configuration is simpler than purely backstepping-based designs, it remains technically demanding in terms of implementation and fine-tuning, particularly during rapid operational transitions where coordination between controllers becomes critical. Furthermore, the PI controller's reliance on linear assumptions and fixed gain parameters limits its adaptability in highly nonlinear or fast-changing environments, often necessitating manual recalibration for sustained performance.

To address limitations highlighted in earlier research, a new hierarchical nested cascade control framework is introduced. This approach aims to overcome previously noted design complexities while delivering a practical and resilient solution. It is specifically tailored for effective DC bus voltage regulation and current management in battery–SC systems, particularly under the variable power loads encountered in real-world driving scenarios. This method capitalizes on the distinct advantages offered by hierarchical nested cascade control based nonlinear control and adaptive PI (API) control that adjusts the parameter of controller in real-time to optimize performance and regulate the DC bus voltage under varying operating conditions or system uncertainties. In contrast, the nested cascade controller is tasked with handling current control for each energy source (FC, SC and battery), owing to its robust capability in managing system uncertainties and ensuring stable performance under dynamic and transient operating conditions. By integrating these two techniques, the control system directly utilizes physical control inputs, thereby eliminating the need for virtual controllers. This simplification reduces internal structural complexity and prevents adverse interactions between control layers. As a result, the system maintains robust operation across varying conditions and ensures seamless transitions between traction and regenerative braking modes.

- A novel hierarchical nested cascade control structure is proposed to reduce design complexity and improve system resilience in FCHEV applications, effectively addressing the shortcomings of traditional cascade control approaches.

- The system integrates nonlinear hierarchical control with API regulation, leveraging a model reference adaptive control (MRAC) framework to enable real-time tuning of control parameters. This architecture ensures optimized DC bus voltage regulation across a wide range of load conditions and operational uncertainties.
- A dedicated nested cascade controller using three distinct backstepping (BS) controller manages current control for FCs, SCs, and batteries, leveraging its robustness against uncertainties and performance during dynamic transitions.
- By directly applying physical control inputs, the approach avoids virtual controllers, simplifying internal architecture and minimizing interference between control layers.
- The overall system ensures stable operation and smooth switching between traction and regenerative braking, even under unpredictable power demands seen in real driving environments.

The structure of the article is as follows: Section 2 details the FCHEV components, Section 3 outlines the proposed EMS, Section 4 presents the input data and simulation outcomes, and Section 5 concludes the study.

2. System framework

In the context of FCHEVs, energy demand is highly variable, influenced by external factors such as road conditions and traffic patterns, as well as internal ones like individual driving habits. Such volatility necessitates an adaptive EMS within multi-source architectures, where power allocation must be strategically distributed in accordance with the transient behavior and response capabilities of each energy source.

The FC, commonly employed as the central power generation unit, is generally optimized for steady-state operation. It lacks the responsiveness needed to meet abrupt power demands, and if forced to do so repeatedly, it can suffer accelerated degradation, resulting in reduced efficiency, power and shortened service life. Consequently, the system integrates complementary energy sources capable of absorbing sudden load changes and responding rapidly to peak demands.

To achieve this hybrid synergy, the proposed system, illustrated schematically in Fig.1, employs a FC connected to the DC bus via an interleaved boost converter, offering improved conversion efficiency and reduced ripple. Parallel

to this, the ESS comprises high-dynamic elements such as battery packs and SC arrays, each interfaced with the DC bus through bidirectional buck-boost converters. These storage units handle fast transients and short-term load variations while supporting the primary unit during demand spikes.

The vehicle's propulsion subsystem includes a three-phase inverter coupled to an AC synchronous motor. This arrangement enables fine-grained control over mechanical output, allowing modulation of speed and torque according to real-time driving conditions and control algorithms. Together, this architecture forms a robust energy framework capable of responding dynamically to the fluctuating power needs of FCHEV operation.

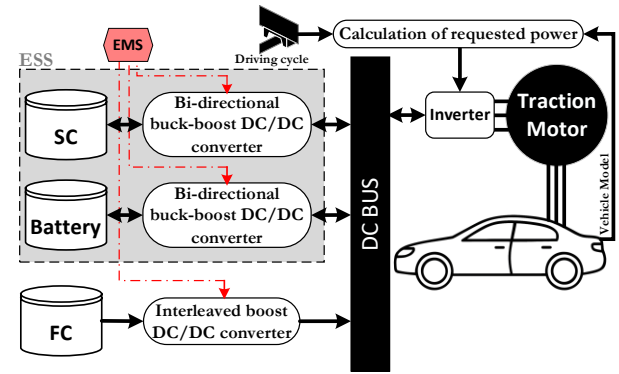


Figure 1: System architecture diagram of a FCHEV with three integrated power sources

2.1. Mathematical Modeling of FC Output Voltage (PEMFC)

The output voltage of a FC (V_{cell}^{FC}) is determined by the Nernst equation, accounting for activation, ohmic, and concentration losses [21]:

$$V_{cell}^{FC} = E_{Nernst} - \eta_{act} - \eta_{ohm} - \eta_{conc} \quad (1)$$

$$E_{Nernst} = E_{cell}^0 + \frac{\kappa T}{2F} \ln \left(\frac{P_{H_2} \cdot \sqrt{P_{O_2}}}{P_{H_2O}} \right) \quad (2)$$

For dry hydrogen supplied at pressure P_{anode} , the partial pressure of hydrogen (P_{H_2}) is calculated using (3). An increase in P_{H_2} enhances the Nernst potential and overall system performance; however, excessively high pressure may induce membrane mechanical stress.

$$P_{H_2} = P_{anode} - P_{H_2O}^{anode} \quad (3)$$

The partial pressure of oxygen (P_{O_2}) is determined using (4). An elevated P_{O_2} improves

reaction kinetics and mitigates activation losses, thereby contributing to enhanced electrochemical performance.

$$P_{O_2} = y_{O_2}(P_{cathode} - P_{H_2O}^{cathode}) \quad (4)$$

The vapor pressure of water within the FC is governed by operating humidity and temperature conditions. Accordingly, the partial pressure of water (P_{H_2O}) is computed using (5) and (6).

$$P_{H_2O} = RH \cdot P_{H_2O}^{sat} \quad (5)$$

$$P_{H_2O}^{sat} = 10^{A - \frac{B}{T+C}} \quad (6)$$

where, A, B, C are substance-specific empirical constants. In this investigation, for temperature in Kelvin and saturated water vapor pressure ($P_{H_2O}^{sat}$) in *bar*, these coefficients are defined as: $A = 5.40221$, $B = 1838.675$ and $C = -31.737$.

Due to sluggish electrode kinetics activation losses (η_{act}) are determined as expressed in (7).

$$\eta_{act} = \frac{\kappa T}{\alpha n F} \ln \left(\frac{j}{j_0} \right) \quad (7)$$

Resistive losses (η_{ohm}), commonly referred to as Ohmic losses, arise from the internal resistance within the electrolyte and associated components, as characterized in (8).

$$\eta_{ohm} = j \cdot R_{ohm}^{FC} \quad (8)$$

Mass transport limitations at high current densities can be defined as follows:

$$\eta_{conc} = \frac{\kappa T}{n F} \ln \left(1 - \frac{j}{j_L} \right) \quad (9)$$

Combining all terms in (1), (2), (7)-(9) yields:

$$V_{cell}^{FC} = E_{Nernst} - \frac{\kappa T}{n F} \left[\frac{1}{\alpha} \ln \left(\frac{j}{j_0} \right) + \ln \left(1 - \frac{j}{j_L} \right) \right] - (j \cdot R_{ohm}^{FC}) \quad (10)$$

2.2. Mathematical Modeling of Lithium-ion (Li-ion) Batteries

The SOC represents the remaining charge in the battery as a percentage of its total capacity. It is computed using the Coulomb counting method with possible corrections for efficiency and aging [22]:

$$SOC(t) = SOC_0 - \frac{1}{Q_{Bat}^{nom}} \int_0^t \eta_C \cdot I_{Bat}(t) dt \quad (11)$$

where, η_C is the coulombic efficiency and considered 0.98 for a typical Li-ion battery [23].

The open-circuit voltage (OCV), denoted as V_{OC}^{Bat} , represents the battery's equilibrium voltage corresponding to a specific SOC. Its behavior is inherently nonlinear and can be mathematically characterized by (12).

$$V_{OC}^{Bat}(SOC) = a + b \cdot SOC + c \cdot e^{d \cdot SOC} \quad (12)$$

where the fitted coefficients $a = 3$, $b = 0.6$, $c = 0.2$, and $d = -5$ are calibrated for a typical Li-ion battery [23].

The actual terminal voltage of the battery under load, denoted as V_T^{Bat} , is influenced by both instantaneous and transient phenomena [24]. Specifically, it accounts for: (1) Ohmic drop, resulting from internal resistance and manifesting as an immediate voltage reduction upon load application, and (2) Polarization effects, encompassing slower electrochemical dynamics that contribute to the transient voltage response. Mathematically, this relationship can be represented as:

$$V_T^{Bat} = V_{OC}^{Bat}(SOC) - I_{Bat} R_0 - V_{RC1} - V_{RC2} \quad (13)$$

In the aforementioned expression, V_T^{Bat} accounts for three key components: (1) Ohmic loss ($I_{Bat} \cdot R_0$): Represents the instantaneous voltage drop due to the internal resistance R_0 . This parameter is typically measured using current pulse tests under controlled conditions; (2) Polarization voltage (V_{RC1}): Captures the short-term transient response arising from charge transfer kinetics. It is commonly modeled as a first-order RC circuit, reflecting the electrochemical dynamics during load transitions (see (14)); (3) Diffusion voltage (V_{RC2}): Reflects long-term electrochemical dynamics arising from ion diffusion within the electrolyte. As presented in (15), this behavior is commonly captured using a second RC circuit, supplementing the short-term transient model to account for gradual voltage evolution under sustained load conditions

$$V_{RC1} = I_{Bat} \cdot R_1 (1 - e^{-t/\tau_1}) \quad (14)$$

$$V_{RC2} = I_{Bat} \cdot R_2 (1 - e^{-t/\tau_2}) \quad (15)$$

where, $\tau_1 = R_1 C_1$ and $\tau_2 = R_2 C_2$.

For simulation and control purposes, the equivalent circuit model can be reformulated in state-space representation, as presented in (16) and (17). This form enables systematic analysis and design of control strategies, facilitating numerical implementation in dynamic environments. Fig. 2 presents the battery modeling circuit diagram, constructed based on the previously described modeling approach.

$$\frac{dV_{RC1}}{dt} = \frac{I_{Bat}}{C_1} - \frac{V_{RC1}}{R_1 C_1} \quad (16)$$

$$\frac{dV_{RC2}}{dt} = \frac{I_{Bat}}{C_2} - \frac{V_{RC2}}{R_2 C_2} \quad (17)$$

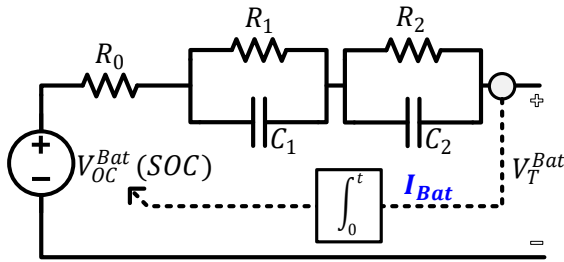


Figure 2: Modeling of Li-ion Battery cells

2.3. Fundamental Models of SCs

The two-branch RC model is commonly employed to characterize the dual charge storage mechanisms in SCs, capturing both the rapid (immediate) and slower (diffusion-dependent) electrochemical dynamics. Fig. 3 presents the SC modeling circuit diagram. The equivalent series resistance R_{SC1} models the fast response, while the capacitance C_{SC1} accounts for surface charge accumulation via the double-layer effect. Conversely, the delayed charge branch (slow dynamics) is characterized by R_{SC2} , representing diffusion resistance in porous electrodes, and C_{SC2} , capturing deep charge storage within the electrode pores. In addition, the leakage resistance R_{SCL} is placed in parallel with C_{SC2} to model the self-discharge phenomenon, characterized by a gradual voltage decay during idle periods. The internal resistance R_{SCS} comprises contributions from both the electrolyte and the contact interfaces between the electrodes and current collectors, and is responsible for the instantaneous voltage drop observed upon current application (see (18)). It is important to note that the parameters of this model, particularly the resistances R_{SCS} , R_{SC1} , R_{SC2} , and the capacitances C_{SC1} , C_{SC2} , are strongly influenced by operational conditions such as temperature. While the simulations in this study utilize parameter values representative of a standard operating temperature, the model's structure is inherently suitable for analyzing thermal effects. The

dependency of these parameters on temperature can be incorporated based on empirical characterization, allowing the model to predict SC behavior across a wider range of environmental scenarios.

$$V_{RS}(t) = I(t) \cdot R_{SCS}(T) \quad (18)$$

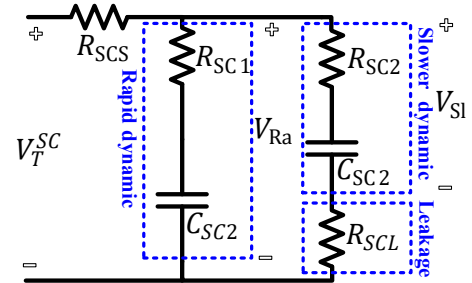


Figure 3: Modeling of SC cells

The fast charging/discharging dynamics are characterized by the time constant $\tau_{SC1} = R_{SC1}C_{SC1}$, as presented in (19), while the slower internal charge redistribution is governed by the time constant $\tau_{SC2} = R_{SC2}C_{SC2}$, detailed in (20).

$$V_{Ra}(t) = I_{SC1}(t)R_{SC1}(T) + \frac{1}{C_{SC1}(T)} \int I_{SC1}(t) dt \quad (19)$$

$$V_{Sl}(t) = I_{SC2}(t)R_{SC2}(T) + \frac{1}{C_{SC2}(T)} \int I_{SC2}(t) dt \quad (20)$$

The total current divides among the respective branches, as presented in (21), while the terminal voltage and leakage current are presented in (22) and (23), respectively.

$$I_{SC}(t) = I_{SC1}(t) + I_{SC2}(t) \quad (21)$$

$$V_T^{SC}(t) = I_{SC}(t)R_{SCS}(T) + V_{C_{SC1}}(t) + V_{C_{SC2}}(t) \quad (22)$$

$$I_{SCL}(t) = \frac{V_{C_{SC2}}(t)}{R_{SCL}(T)} \quad (23)$$

For the fast and slow branch charging processes, the respective intended voltages are presented in (24) and (25). By incorporating the initial voltage drop across the series resistance, given by $V_{SC}(0^+) = I_{SC0}R_{SCS}$, the total voltage at the SC terminal can then be expressed as (26).

$$V_{C_{SC1}}(t) = I_{SC0}R_{SC1}(T)(1 - e^{-t/\tau_{SC1}}) \quad (24)$$

$$V_{C_{SC2}}(t) = I_{SC0} R_{SC2}(T)(1 - e^{-t/\tau_{SC2}}) \quad (25)$$

$$V_T^{SC}(t) = I_{SC0} [R_{SCS}(T) + R_{SC1}(T)(1 - e^{-t/\tau_{SC1}}) + R_{SC2}(T)(1 - e^{-t/\tau_{SC2}})] \quad (26)$$

2.4. Bidirectional buck-boost DC-DC converter

Fig. 4 illustrates the comprehensive design and overall structural configuration of the bidirectional buck-boost DC-DC converter. This power converter positioned near the two input sources (battery and SC) functions in boost mode during energy discharge ($I_{in-Ref} > 0$) when switch S_1 is activated while S_2 remains inactive. Conversely, if S_1 is turned off and S_2 is engaged, the converter shifts to buck mode, thereby charging the sources ($I_{in-Ref} < 0$). To formally characterize these operational states, charging and discharging, a binary variable β is introduced as follows [25]:

$$\beta = \begin{cases} 0, & I_{in-Ref} < 0 \\ 1, & I_{in-Ref} > 0 \end{cases} \quad (27)$$

The parameter I_{in-Ref} represents the reference current drawn from the input energy sources, serving as a key control variable. Under the boost configuration, corresponding to the discharging mode, the system's dynamic response is governed by the coupled nonlinear differential equations outlined in expressions (28) and (29), enabling precise modeling.

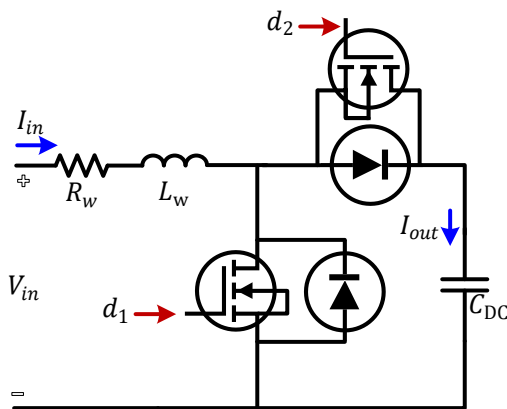


Figure 4: Overall structural configuration of the bidirectional buck-boost DC-DC converter

$$\frac{di_{in}}{dt} = \frac{V_{in}}{L_w} - \frac{R_w}{L_w} i_{in} - (1 - d_1) \frac{V_{DC}}{L_w} \quad (28)$$

$$\frac{dV_{DC}}{dt} = (1 - d_1) \frac{i_{in}}{C_{DC}} - \frac{i_{out}}{C_{DC}} \quad (29)$$

In this context, i_{in} denotes the current entering the system, while V_{in} and V_{DC} correspond to the source voltage and the DC bus voltage, respectively. The control signal is represented by d_1 , and i_{out} signifies the converter's output current. The parameters L_w and R_w refer to the input-side wiring inductance and resistance of the energy sources, respectively. C_{DC} indicates the capacitance of the DC bus.

The governing equations for buck-mode dynamics during charging are given by:

$$\frac{di_{in}}{dt} = \frac{V_{in}}{L_w} - \frac{R_w}{L_w} i_{in} - d_2 \frac{V_{DC}}{L_w} \quad (30)$$

$$\frac{dV_{DC}}{dt} = d_2 \frac{i_{in}}{C_{DC}} - \frac{i_{out}}{C_{DC}} \quad (31)$$

Here, d_2 denotes the control input associated with buck-mode operation. A unified global model for the converter is derived by combining the charging and discharging modes as follows:

$$\frac{di_{in}}{dt} = \frac{V_{in}}{L_w} - \frac{R_w}{L_w} i_{in} - \delta \frac{V_{DC}}{L_w} \quad (32)$$

$$\frac{dV_{DC}}{dt} = \delta \frac{i_{in}}{C_{DC}} - \frac{i_{out}}{C_{DC}} \quad (33)$$

Here, δ is a final control signal defined as:

$$\delta = \beta(1 - d_1) + (1 - \beta)d_2 \quad (34)$$

This approach ensures smooth switching between charge and discharge states, with sustained regulation of the system's dynamic behavior. Consequently, the input expressions for the battery and SC can be reformulated, as indicated in equations (35)-(40). Eventually, the terminal value of the ESS current is determined using (41), and the global model for ESS is obtained in (42). In the present investigation, the ESS exhibits a multi-input multi-output (MIMO) architecture with dynamically nonlinear behavior, which substantially increases the complexity of achieving control objectives. Moreover, regulating the output power of the primary source (FC) constitutes a core control objective, yet the system's inherent nonlinearities and interdependencies further intensify the associated challenges.

$$\frac{dI_{Bat}}{dt} = \frac{V_T^{Bat}}{L_{w1}} - \frac{R_{w1}}{L_{w1}} I_{Bat} - \delta_{Bat} \frac{V_{DC}}{L_{w1}} \quad (35)$$

$$\frac{dV_{DC}}{dt} = \delta_{Bat} \frac{I_{Bat}}{C_{DC}} - \frac{i_{out1}}{C_{DC}} \quad (36)$$

$$\delta_{Bat} = \beta_{Bat}(1 - d_1^{Bat}) + (1 - \beta_{Bat})d_2^{Bat} \quad (37)$$

$$\frac{dI_{SC}}{dt} = \frac{V_{FC}^{SC}}{L_{w2}} - \frac{R_{w2}}{L_{w2}} I_{SC} - \delta_{SC} \frac{V_{DC}}{L_{w2}} \quad (38)$$

$$\frac{dV_{DC}}{dt} = \delta_{SC} \frac{I_{SC}}{C_{DC}} - \frac{i_{out2}}{C_{DC}} \quad (39)$$

$$\delta_{SC} = \beta_{SC}(1 - d_1^{SC}) + (1 - \beta_{SC})d_2^{SC} \quad (40)$$

$$i_{out}^{ESS} = i_{out1} + i_{out2} \quad (41)$$

$$\frac{dV_{DC}}{dt} = \delta_{Bat} \frac{I_{Bat}}{C_{DC}} - \frac{i_{out}^{ESS} - \delta_{SC} I_{SC}}{C_{DC}} \quad (42)$$

2.5. Interleaved boost DC/DC converter

As depicted in Fig. 5, the interleaved boost DC/DC converter serves as the primary power unit for the vehicle's input stage [26]. It functions in continuous conduction mode (CCM), enabling efficient regulation and amplification of the FC output voltage. The analysis is divided into two cases based on the switching states.

Case 1: When switch S_1 is activated (ON) and S_2 is deactivated (OFF), S_1 provides a closed path while diode D_1 becomes reverse-biased and remains non-conductive. Conversely, with S_2 open, diode D_2 is forward-biased and conducts current. Consequently, inductor L_{FC1} is energized through the input voltage V_{cell}^{FC} , while the stored energy in L_{FC2} is transferred to the output circuit via diode D_2 . The analytical expressions corresponding to this operation mode are detailed in (43)-(45).

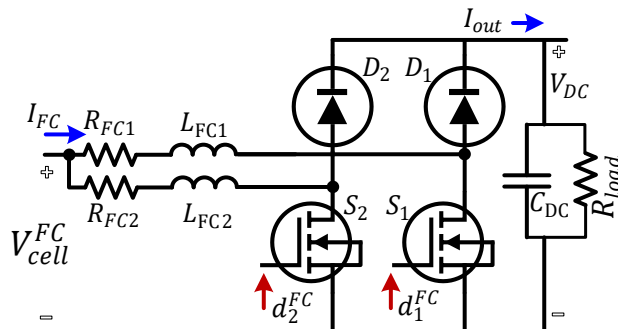


Figure 5: Overall structural configuration of the interleaved boost DC/DC converter

$$\frac{di_{L_{FC1}}}{dt} = \frac{V_{cell}^{FC}}{L_{FC1}} \quad (43)$$

$$\frac{di_{L_{FC2}}}{dt} = \frac{V_{cell}^{FC} - V_{DC}}{L_{FC2}} \quad (44)$$

$$\frac{dV_{DC}}{dt} = \frac{i_{L_{FC2}}}{C_{DC}} - \frac{V_{DC}}{R_{load}C_{DC}} \quad (45)$$

Case 2: When switch S_1 is turned off and S_2 is activated, S_1 remains in the open state, enabling diode D_1 to conduct. In contrast, the closed state of S_2 renders diode D_2 reverse-biased and thus non-conductive. Under these conditions, inductor L_2 is charged by the FC voltage V_{cell}^{FC} , while the stored energy in inductor L_1 is delivered to the output through diode D_1 . The corresponding governing equation for this operating mode is reformulated as:

$$\frac{di_{L_{FC1}}}{dt} = \frac{V_{cell}^{FC} - V_{DC}}{L_{FC1}} \quad (46)$$

$$\frac{di_{L_{FC2}}}{dt} = \frac{V_{cell}^{FC}}{L_{FC2}} \quad (47)$$

$$\frac{dV_{DC}}{dt} = \frac{i_{L_{FC1}}}{C_{DC}} - \frac{V_{DC}}{R_{load}C_{DC}} \quad (48)$$

Using state-space averaging, the unified converter dynamics are represented by (49) and (50), from which the output voltage is subsequently derived as expressed in (51).

$$L_{FC1} \frac{di_{L_{FC1}}}{dt} = V_{cell}^{FC} - (1 - d_1^{FC})V_{DC} \quad (49)$$

$$L_{FC2} \frac{di_{L_{FC2}}}{dt} = V_{cell}^{FC} - (1 - d_2^{FC})V_{DC} \quad (50)$$

$$C_{DC} \frac{dV_{DC}}{dt} = (1 - d_1^{FC})i_{L_{FC1}} + (1 - d_2^{FC})i_{L_{FC2}} - \frac{V_{DC}}{R_{load}} \quad (51)$$

3. Hierarchical Nested Cascade Control Framework

The proposed strategy for energy management of FCEVs integrates a FC as the primary power source along with an ESS. Within the ESS, batteries offer high energy density but limited power output, whereas SCs deliver superior power density and longevity, though at the expense of energy capacity. This hybrid configuration is designed to improve FC operational stability and efficiency, while also optimizing the ESS by

leveraging the SC's rapid response to peak power demands and assigning smoother load profiles to the battery. Central to this framework is the implementation of a dynamic power distribution method combined with a resilient control mechanism, enabling effective handling of transient load conditions.

The hierarchical nested cascade control framework illustrated in Fig. 6 is structured across three coordinated layers: an outer control level (OCL) governed by the adaptive API controller, and two inner layers, namely, the middle control level (MCL) and inner control level (ICL), each implemented using BS controllers. The primary objective of the API controller is to regulate the DC bus voltage, ensuring system-wide voltage stability under varying load conditions. In contrast, the BS controllers are responsible for precise current management of both the FC and the ESS, which includes the battery and SC.

This multi-tiered configuration enables dynamic and decoupled control of power flow across the system. The control sequence begins by applying the backstepping technique to govern the current profiles of the FC and ESS components individually. By isolating control responsibilities across these nested levels, the framework enhances robustness against uncertainties and improves adaptability to transient operating states. Furthermore, this approach facilitates modular expansion and allows for the integration of advanced control policies without compromising overall system coherence. The synergy between voltage regulation and current control mechanisms enables stable and responsive power management, which is essential for real-world FCHEV applications where load variability and nonlinear dynamics are prevalent.

BS nonlinear control is fundamentally a recursive design methodology wherein the control law is constructed incrementally. At each stage of the synthesis process, a specific system state is stabilized by treating the subsequent state as a virtual control input. This iterative approach results in the formulation of a stabilizing control function that systematically drives the system toward its desired equilibrium state, typically a stable closed-loop configuration. The recursive nature of BS facilitates a structured and modular control law derivation, making it particularly effective for systems exhibiting hierarchical dynamics or strong nonlinearities. Stability throughout the control design process is rigorously ensured by employing Lyapunov-based functions, which guide the selection of control

parameters at each step and verify convergence toward the desired behavior [27].

In the context of regulating the DC bus voltage and achieving the control objectives of the proposed framework, the initial phase involves defining an appropriate tracking error for FC system. This error quantifies the deviation between the actual and target voltage trajectories and forms the basis for subsequent control synthesis. The first tracking error for FC, central to the backstepping procedure, is defined as follows:

$$\varepsilon_{FC,1} = I_{FC} - I_{FC}^{Ref} \quad (52)$$

Differentiating (52) and substituting into (49) and (50) yields the following expression for the error dynamics:

$$\begin{aligned} \frac{d\varepsilon_{FC,1}}{dt} &= \left(\frac{di_{L_{FC1}}}{dt} + \frac{di_{L_{FC2}}}{dt} \right) - \frac{dI_{FC}^{Ref}}{dt} \\ &= \left(\frac{V_{cell}^{FC} - (1 - d_1^{FC})V_{DC}}{L_{FC1}} + \frac{V_{cell}^{FC} - (1 - d_2^{FC})V_{DC}}{L_{FC2}} \right) - \frac{dI_{FC}^{Ref}}{dt} \end{aligned} \quad (53)$$

To assess system stability and convergence, a Lyapunov candidate function is introduced and defined as follows:

$$\vartheta_{FC,1} = \frac{1}{2}(\varepsilon_{FC,1})^2 \quad (54)$$

Based on Lyapunov's stability theorem, the system exhibits asymptotic stability if derivative of the $\vartheta_{FC,1}$ remains negative. Accordingly, $\frac{d\vartheta_{FC,1}}{dt}$ can be reformulated as follows:

$$\begin{aligned} \frac{d\vartheta_{FC,1}}{dt} &= \varepsilon_{FC,1} \times \frac{d\varepsilon_{FC,1}}{dt} \\ &= \varepsilon_{FC,1} \left(\left(\frac{V_{cell}^{FC} - (1 - d_1^{FC})V_{DC}}{L_{FC1}} + \frac{V_{cell}^{FC} - (1 - d_2^{FC})V_{DC}}{L_{FC2}} \right) - \frac{dI_{FC}^{Ref}}{dt} \right) \end{aligned} \quad (55)$$

Reformulate the (55) to reflect virtual control, so, the expression is modified as follows:

$$\frac{d\vartheta_{FC,1}}{dt} = \varepsilon_{FC,1} \left(\frac{V_{cell}^{FC}(L_{FC1} + L_{FC2})}{L_{FC1}L_{FC2}} - \frac{V_{DC}}{L_{FC1}L_{FC2}} (L_{FC2}(1 - d_1^{FC}) + L_{FC1}(1 - d_2^{FC})) - \frac{dI_{FC}^{Ref}}{dt} \right) \quad (56)$$

Selecting $\frac{V_{DC}}{L_{FC1}L_{FC2}}$ function as a virtual control parameter (γ) to ensure that $\frac{d\vartheta_{FC,1}}{dt}$ remains negative. Consequently, we derive the following:

$$\begin{aligned} \frac{V_{DC}}{L_{FC1}L_{FC2}} &= \gamma \\ P_1 \varepsilon_{FC,1} + \frac{V_{cell}^{FC}(L_{FC1} + L_{FC2})}{L_{FC1}L_{FC2}} - \frac{dI_{FC}^{Ref}}{dt} &= \frac{P_1 \varepsilon_{FC,1} + \frac{V_{cell}^{FC}(L_{FC1} + L_{FC2})}{L_{FC1}L_{FC2}} - \frac{dI_{FC}^{Ref}}{dt}}{L_{FC2}(1 - d_1^{FC}) + L_{FC1}(1 - d_2^{FC})} \end{aligned} \quad (57)$$

where P_1 denotes a design parameter that governs the structural configuration of the model.

The subsequent step involves introducing the second error term, defined as follows:

$$\varepsilon_{FC,2} = \frac{V_{DC}}{L_{FC1}L_{FC2}} - \gamma \quad (58)$$

Subsequently, as presented in (59), the term $\frac{d\varepsilon_{FC,2}}{dt}$ is computed by applying (58) and (51).

$$\frac{d\varepsilon_{FC,2}}{dt} = \frac{(1 - d_1^{FC})i_{L_{FC1}} + (1 - d_2^{FC})i_{L_{FC2}}}{C_{DC}L_{FC1}L_{FC2}} - \frac{V_{DC}}{R_{load}C_{DC}L_{FC1}L_{FC2}} - \frac{d\gamma}{dt} \quad (59)$$

Based on (49), (50), (53), and (57), the time derivative of γ is formulated and presented in (60). Consequently, the value of $\frac{d\gamma}{dt}$ is substituted into (59) to evaluate the derivative of the second component of the error term. Subsequently, a composite Lyapunov function is constructed in (61).

$$\vartheta_{FC,2} = \vartheta_{FC,1} + \frac{1}{2}(\varepsilon_{FC,2})^2 \quad (61)$$

Differentiating the function presented in (61) yields the following expression:

$$\frac{d\vartheta_{FC,2}}{dt} = \frac{d\vartheta_{FC,1}}{dt} + \left(\frac{d\varepsilon_{FC,2}}{dt} \times \varepsilon_{FC,2} \right) \quad (62)$$

Taking into account the relationship defined in (55), the following result is obtained:

$$\begin{aligned} \frac{d\vartheta_{FC,2}}{dt} &= \left(\varepsilon_{FC,1} \times \frac{d\varepsilon_{FC,1}}{dt} \right) \\ &+ \left(\varepsilon_{FC,2} \times \frac{d\varepsilon_{FC,2}}{dt} \right) \end{aligned} \quad (63)$$

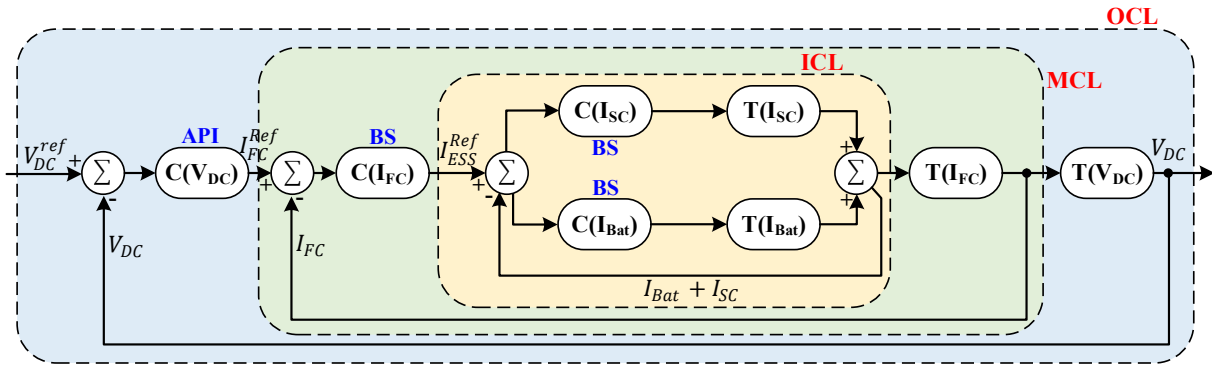


Figure 6: Proposed hierarchical nested cascade control framework

$$\begin{aligned} \frac{d\gamma}{dt} &= \frac{P_1 \left(\left(\frac{V_{cell}^{FC} - (1 - d_1^{FC})V_{DC}}{L_{FC1}} + \frac{V_{cell}^{FC} - (1 - d_2^{FC})V_{DC}}{L_{FC2}} \right) - \frac{dI_{FC}^{Ref}}{dt} \right)}{L_{FC2}(1 - d_1^{FC}) + L_{FC1}(1 - d_2^{FC})} \\ &+ \frac{\frac{(L_{FC1} + L_{FC2})}{L_{FC1}L_{FC2}} \left(\frac{(1 - d_1^{FC})i_{L_{FC1}} + (1 - d_2^{FC})i_{L_{FC2}} - \frac{V_{DC}}{R_{load}}}{C_{DC}} \right) - \frac{d^2 I_{FC}^{Ref}}{dt^2}}{L_{FC2}(1 - d_1^{FC}) + L_{FC1}(1 - d_2^{FC})} \end{aligned} \quad (60)$$

By strategically adding and subtracting a specific term to regulate the second component, (64) can be reformulated as follows:

$$\begin{aligned} \frac{d\vartheta_{FC,2}}{dt} = & \left(\varepsilon_{FC,1} \times \frac{d\varepsilon_{FC,1}}{dt} \right) \\ & + \left(\varepsilon_{FC,2} \times \frac{d\varepsilon_{FC,2}}{dt} \right) \\ & + P_2 \varepsilon_{FC,2}^2 - P_2 \varepsilon_{FC,2}^2 \end{aligned} \quad (64)$$

where $P_2 > 0$ denotes a design parameter for second term that governs the structural configuration of the model.

To guarantee the negativity of $\frac{d\vartheta_{FC,2}}{dt}$, (65) must be satisfied. Also, the control inputs d_1^{FC} and d_2^{FC} should be redefined as new control variables to ensure the desired dynamic behavior to meet the stability criteria under varying operating conditions.

$$\varepsilon_{FC,1} \times \frac{d\varepsilon_{FC,1}}{dt} + \varepsilon_{FC,2} \times \frac{d\varepsilon_{FC,2}}{dt} + P_2 \varepsilon_{FC,2}^2 < 0 \quad (65)$$

Once the FC output has been regulated to stabilize the DC voltage, attention shifts to managing the output current of the ESS. Based on the output of the MCL, the reference current for the ESS is determined to control the output of ESS. However, achieving this objective necessitates a nonlinear model that characterizes the relationship between the input currents of each ESS, namely I_{Bat} and I_{SC} , and the associated control variables δ_{Bat} and δ_{SC} . To initiate the control process, the tracking errors are first defined as follows:

$$\varepsilon_{Bat,3} = I_{Bat} - I_{Bat}^{Ref} \quad (66)$$

$$\varepsilon_{SC,4} = I_{SC} - I_{SC}^{Ref} \quad (67)$$

By differentiating the error expressions in (66) and (67), and incorporating the system dynamics from (35) and (38), the resulting dynamic error formulations are derived as follows:

$$\begin{aligned} \frac{d\varepsilon_{Bat,3}}{dt} = & \frac{V_T^{Bat}}{L_{w1}} - \frac{R_{w1}}{L_{w1}} I_{Bat} - \delta_{Bat} \frac{V_{DC}}{L_{w1}} \\ & - \frac{dI_{Bat}^{Ref}}{dt} \end{aligned} \quad (68)$$

$$\frac{d\varepsilon_{SC,4}}{dt} = \frac{V_T^{SC}}{L_{w2}} - \frac{R_{w2}}{L_{w2}} I_{SC} - \delta_{SC} \frac{V_{DC}}{L_{w2}} - \frac{dI_{SC}^{Ref}}{dt} \quad (69)$$

In accordance with the control requirements provided for FC unit, Lyapunov candidate functions are formulated for both the battery and SC units to assess system stability and convergence. These functions are defined as follows:

$$\vartheta_{Bat,3} = \frac{1}{2} (\varepsilon_{Bat,3})^2 \quad (70)$$

$$\vartheta_{SC,4} = \frac{1}{2} (\varepsilon_{SC,4})^2 \quad (71)$$

Based on Lyapunov's stability criterion, a system achieves asymptotic stability when the derivatives of the Lyapunov candidate functions, $\vartheta_{Bat,3}$ and $\vartheta_{SC,4}$, are strictly negative. To satisfy this requirement, these derivatives are deliberately set to $-P_3 \varepsilon_{Bat,3}^2$ and $-P_4 \varepsilon_{SC,4}^2$, respectively, where P_3 and P_4 denote positive design parameters, and $\varepsilon_{Bat,3}$, $\varepsilon_{SC,4}$ correspond to the associated error signals. By performing differentiation on (70) and (71), the following expressions are derived:

$$\frac{d\vartheta_{Bat,3}}{dt} = \varepsilon_{Bat,3} \times \frac{d\varepsilon_{Bat,3}}{dt} = -P_3 \varepsilon_{Bat,3}^2 \quad (72)$$

$$\frac{d\vartheta_{SC,4}}{dt} = \varepsilon_{SC,4} \times \frac{d\varepsilon_{SC,4}}{dt} = -P_4 \varepsilon_{SC,4}^2 \quad (73)$$

Substituting the expressions from (68) and (69) into (72) and (73) yields the following relationships:

$$\begin{aligned} \delta_{Bat} = & \frac{L_{w1}}{V_{DC}} \left(\frac{V_T^{Bat}}{L_{w1}} - \frac{R_{w1}}{L_{w1}} I_{Bat} - \frac{dI_{Bat}^{Ref}}{dt} \right. \\ & \left. + P_3 \varepsilon_{Bat,3} \right) \end{aligned} \quad (74)$$

$$\begin{aligned} \delta_{SC} = & \frac{L_{w2}}{V_{DC}} \left(\frac{V_T^{SC}}{L_{w2}} - \frac{R_{w2}}{L_{w2}} I_{SC} - \frac{dI_{SC}^{Ref}}{dt} \right. \\ & \left. + P_4 \varepsilon_{SC,4} \right) \end{aligned} \quad (75)$$

Regarding the global asymptotic stability of the overall system, it can be inferred from (55), (72), and (73) that the corresponding expressions are strictly negative, provided that P_1 , P_2 , P_3 , and P_4 are positive. Consequently, by applying Lyapunov stability theory, the closed-loop control strategy for the FCHEV power system ensures global asymptotic stability, as rigorously demonstrated and validated in (76).

$$\begin{aligned} \frac{\partial \vartheta_{sys}}{\partial t} &= \frac{d\vartheta_{FC,1}}{dt} + \frac{d\vartheta_{FC,2}}{dt} + \frac{d\vartheta_{Bat,3}}{dt} + \frac{d\vartheta_{SC,4}}{dt} \\ &= -P_1 \varepsilon_{FC,1}^2 - P_2 \varepsilon_{FC,2}^2 - P_3 \varepsilon_{Bat,3}^2 - P_4 \varepsilon_{SC,4}^2 \end{aligned} \quad (76)$$

In FCHEV systems, ensuring the stability of the DC bus voltage is essential for reliable operation. Hence, the subsequent step involves designing the OCL to regulate the DC bus voltage, even in the presence of dynamic load variations. Although PI controllers are widely employed for this purpose, their effectiveness may deteriorate in the presence of load fluctuations, parameter uncertainties, or external disturbances. To enhance robustness, MRAC mechanism can be implemented to continuously tune the PI gains K_p and K_i , thereby maintaining consistent voltage regulation under varying operating conditions. The primary control objective of the OCL is presented in (77).

$$\varepsilon_V = V_{DC} - V_{DC}^{ref} \quad (77)$$

Taking the derivative of equation (77) results in:

$$\frac{d\varepsilon_V}{dt} = \frac{dV_{DC}}{dt} - \frac{dV_{DC}^{ref}}{dt} \quad (78)$$

Taking into account the DC bus capacitor and total input currents, the expression may be reformulated as:

$$\frac{d\varepsilon_V}{dt} = \frac{I_{FC} + I_{Bat} + I_{SC} - I_{Load}}{dt} - \frac{dV_{DC}^{ref}}{dt} \quad (79)$$

The API controller generates the input current reference as follows:

$$I_{FC} + I_{Bat} + I_{SC} = K_p \varepsilon_V + K_i \int \varepsilon_V dt \quad (80)$$

The Lyapunov function is constructed to ensure the regulation of the DC bus voltage, as follows:

$$\vartheta_{DC} = \frac{1}{2} \varepsilon_V^2 + \frac{1}{2\mu_p} \tilde{K}_p^2 + \frac{1}{2\mu_i} \tilde{K}_i^2 \quad (81)$$

where, $\tilde{K}_p = K_p - K_p^*$ represents error in K_p , $\tilde{K}_i = K_i - K_i^*$ represents error in K_i , and μ_p, μ_i are adaptation gains.

Differentiate ϑ_{DC} and enforce $\frac{d\vartheta_{DC}}{dt} \leq 0$ to derive adaptation laws:

$$\frac{d\vartheta_{DC}}{dt} = \varepsilon_V \times \frac{d\varepsilon_V}{dt} + \frac{1}{\mu_p} \tilde{K}_p \frac{d\tilde{K}_p}{dt} + \frac{1}{\mu_i} \tilde{K}_i \frac{d\tilde{K}_i}{dt} \quad (82)$$

$$\frac{d\tilde{K}_p}{dt} = \mu_p \varepsilon_V^2 \quad (83)$$

$$\frac{d\tilde{K}_i}{dt} = \mu_i \varepsilon_V \int \varepsilon_V dt \quad (84)$$

Consequently, by incorporating relations (79), (80), (83), and (84), relation (82) can be reformulated as:

$$\begin{aligned} \frac{d\vartheta_{DC}}{dt} &= \varepsilon_V \times \left(\frac{K_p \varepsilon_V + K_i \int \varepsilon_V dt - I_{Load}}{dt} \right. \\ &\quad \left. - \frac{dV_{DC}^{ref}}{dt} \right) + \tilde{K}_p \varepsilon_V^2 \\ &\quad + \tilde{K}_i \varepsilon_V \int \varepsilon_V dt \end{aligned} \quad (85)$$

To make adaptation sensitive to error magnitude, normalize gains are as follows:

$$\mu_p = \frac{\sigma_p}{\max \text{ expected } \varepsilon_V^2} \quad (86)$$

$$\mu_i = \frac{\sigma_i}{\max \text{ expected } |\varepsilon_V \cdot \int \varepsilon_V dt|} \quad (87)$$

where σ_p, σ_i denote dimensionless scaling coefficients, assigned values of 0.35 and 0.6, respectively.

4. Simulation and Analysis

To assess the effectiveness of the proposed EMS based on the hierarchical nested cascade control framework, a series of simulations were conducted using the MATLAB/Simulink environment. The system parameters employed in the simulation are summarized in Table 1. Additional general parameters are provided in the last section (see list of symbols). The hybrid powertrain under consideration is configured for a FCHEV, integrating three complementary energy sources: Battery, UC, and FC.

The load profile is intentionally crafted to incorporate abrupt fluctuations in power demand, effectively simulating realistic driving conditions using the standardized WLTC-Class 3 driving cycle, as illustrated by the diverse speed profile shown in Fig. 7. This cycle, characterized by distinct acceleration, deceleration, and idling

phases, imposes diverse transient load patterns on the hybrid energy system and highlights the low, medium, high, and extra-high speed phases used to simulate real-world driving conditions. Throughout the simulation, the DC bus reference voltage is maintained at a constant 380V to ensure consistent baseline conditions for performance evaluation. The primary objective of this analysis is to investigate the transient response of the FCHEV system under dynamic load scenarios. Particular attention is given to the voltage and current stability during rapid load transitions. The proposed EMS demonstrates robust control performance, effectively coordinating power distribution among the three energy sources and minimizing voltage deviations and current overshoots. The findings presented in this section highlight the robustness and efficacy of the proposed control framework in significantly improving system resilience, promoting dynamic adaptability to varying operational conditions, and optimizing energy utilization within FCHEV architectures. By seamlessly integrating adaptive control strategies with real-time system feedback, the framework demonstrates its potential to address the multifaceted challenges of modern FCHEVs, thereby contributing to enhanced performance, sustainability, and reliability in next-generation transportation technologies.

Table 1: System parameters of the hybrid EMS under study

Symbol	Value
R_0 (ch, dch)	(0.85m Ω , 0.7m Ω)
R_1	35 m Ω
R_2	380 m Ω
C_1	90 F
C_2	450 F
Q_{Bat}^{nom}	40 kWh
V_{OC}^{Bat} (SOC = 100)	260 V
R_{SCS}	0.5 m Ω
R_{SCL}	30 Ω
R_{SC1}	8.5 m Ω
R_{SC2}	65 m Ω
C_{SC1}	60 F
C_{SC2}	2400 F
R_{w1}, R_{w2}	0.5 m Ω
L_{w1}, L_{w2}	5 mH
R_{FC1}, R_{FC2}	1 m Ω
L_{FC1}, L_{FC2}	1.6 mH
R_{ohm}^{FC}	20 m Ω
T	334 K
P_1, P_2, P_3, P_4	2800, 2500, 1500, 2000
C_{DC}	30 mF
V_{DC}^{ref}	380 V
P_{anode}	2 atm
$P_{cathode}$	1.5 atm
RH	50 %

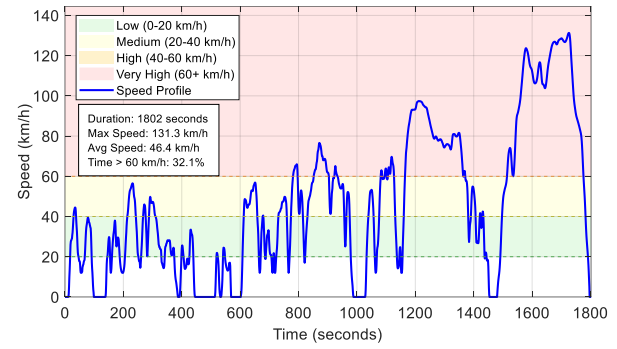


Figure 7: Speed-time profile of the standardized WLTC-Class 3 driving cycle, illustrating the distinct phases used to simulate realistic driving conditions.

In the present investigation the total instantaneous electric power demand of an FCHEV is determined by the product of the total tractive force F_{total} acting on the vehicle and its velocity v , and also overall drivetrain efficiency $\eta_{drivetrain}$ (0.85).

$$P_{FCHEV} = \frac{F_{total}}{\eta_{drivetrain}} \cdot v \quad (88)$$

The total tractive force comprises several components, including gravitational force due to road slope, inertial force, rolling resistance, aerodynamic drag, and regenerative braking effects. These forces can be expressed as:

$$F_{total} = F_{slope} + F_{inertial} + F_{friction} + F_{drag} + F_{regen} \quad (89)$$

Combining these components, the total electric power demand is considered as follows:

$$P_{EV} = v \cdot \left(\frac{mgsin(\theta) + ma + mgC_r cos(\theta)}{\eta_{drivetrain}} + \frac{\frac{1}{2}\rho C_d A v^2 - \eta_{regen} ma}{\eta_{drivetrain}} \right) \quad (90)$$

Here, a denotes the vehicle's linear acceleration (positive during acceleration, negative during deceleration). The rolling resistance coefficient C_r depends on tire characteristics and road surface conditions, in this study $C_r = 0.01$. Also, $m = 1500$ kg, $g = 9.81$ m/s², $\rho = 1.225$ kg/m³, $C_d = 0.3$, $A = 2.5$ m². Moreover, during deceleration ($a < 0$), regenerative braking recovers a fraction of kinetic energy. In doing so,

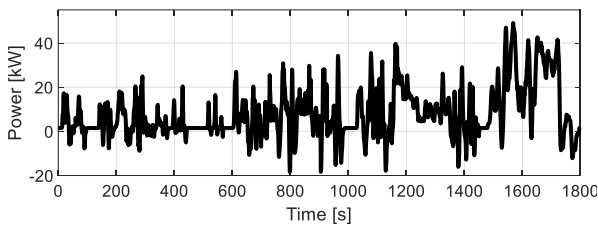


Figure 8: Total instantaneous electric power demand of the FCHEV under the WLTC-Class 3 driving cycle.

η_{regen} represents the regenerative braking efficiency, which is typically set to 0.75.

Based on the prescribed drive cycle and the formulation of vehicle longitudinal dynamics, the total instantaneous electric power demand is determined as presented in Fig. 8.

To assess the performance and advantages of the proposed energy management strategy for hybrid electric vehicles, the results are systematically compared with two established benchmark approaches, as outlined below:

- **Case 1:** Application of the proposed hierarchical nested cascade control framework.
- **Case 2:** Deployment of a data-driven reinforcement-learning-based on the type-1 fuzzy logic controller, as described in [13].
- **Case 3:** Utilization of a real-time control strategy, as presented in [10].

In this study, the current profiles and power distribution among the three energy sources, battery, SC, and FC, within an FCHEV were analyzed under three distinct EMSs, referred to as Case 1, Case 2, and Case 3. Case 1 consistently demonstrated superior performance across multiple metrics. Specifically, as shown in Fig. 9, it exhibited the lowest current ripple, which is critical for enhancing the longevity and efficiency of power electronic components. Additionally, Case 1 minimized the instantaneous power demand from both the battery and the SC, thereby reducing thermal stress and improving overall energy efficiency. Notably, this strategy also facilitated a more effective and sustained utilization of the FC's capacity, ensuring that its output was leveraged optimally without inducing excessive transients. In contrast, Case 2 showed less favorable results, with higher current ripple and greater reliance on the battery and SC, leading to increased strain on these components. Case 3 performed marginally better than Case 2 but still fell short of the performance achieved by Case 1. These findings underscore the robustness of Case

1 as the most balanced and efficient strategy, offering improved dynamic response and better resource allocation among the available energy sources.

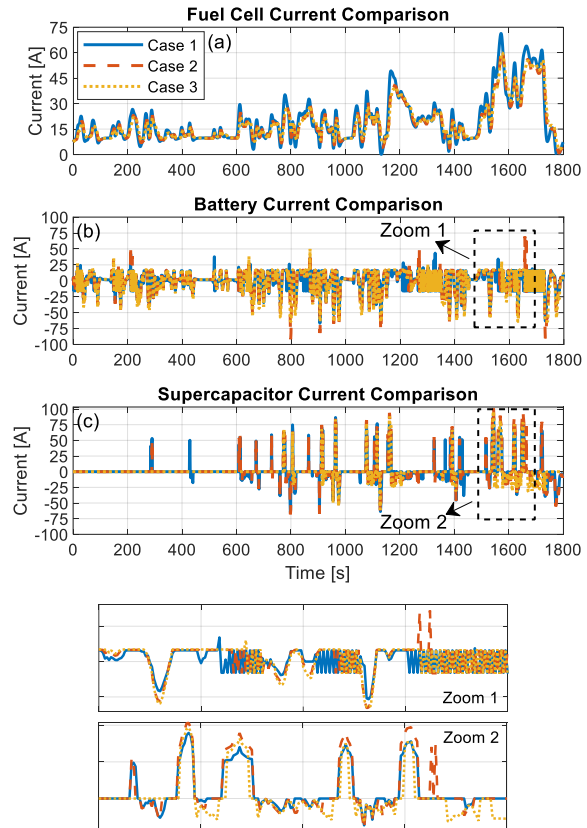


Figure 9: Total current of each power sources based on electric power demand of the FCHEV; (a) FC, (b) Battery, and (c) SC

The power allocation strategy in Case 1 is designed to distribute the load demand more evenly across the available energy sources, thereby significantly reducing the instantaneous power spikes typically imposed on the battery and SC. As illustrated in Fig. 10, by smoothing the power flow and avoiding abrupt transients, Case 1 effectively mitigates electrical and thermal stress on these components, which is crucial for prolonging their operational lifespan and maintaining system reliability. Moreover, this strategy allows the FC to operate closer to its optimal efficiency range, with fewer idle periods and more consistent power output, leading to enhanced FC utilization (see Fig. 11). In contrast, Case 2 exhibits a less coordinated power distribution, resulting in frequent high-power demands from the battery and SC, which not only accelerates degradation but also limits the FC's contribution to the overall energy supply. Case 3 performs marginally better than Case 2 in terms of FC engagement, yet still suffers from inefficient load sharing and elevated stress levels on the auxiliary sources. These comparative results

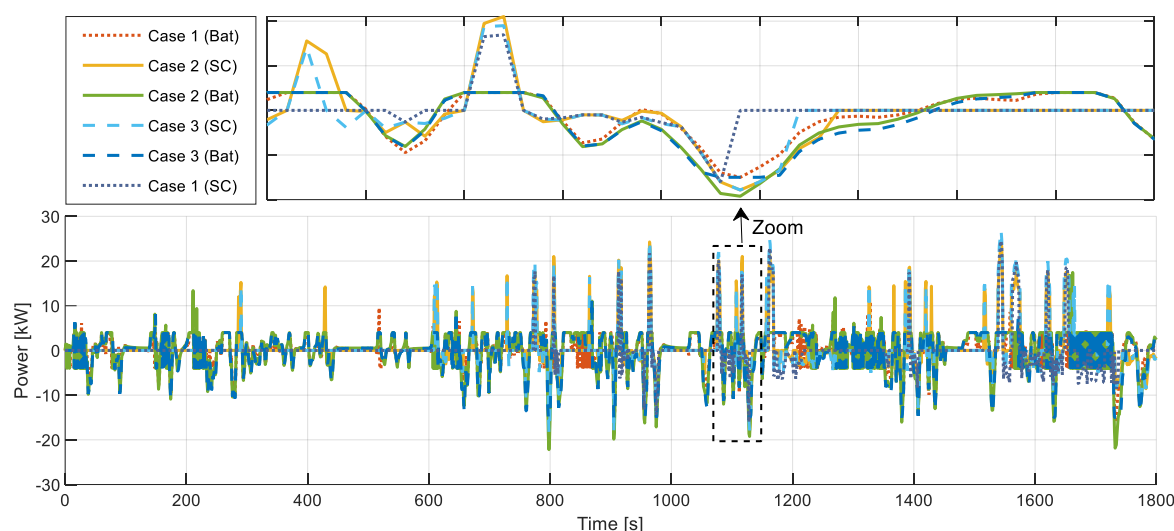


Figure 10: Total power of each battery and SC sources based on electric power demand of the FCHEV

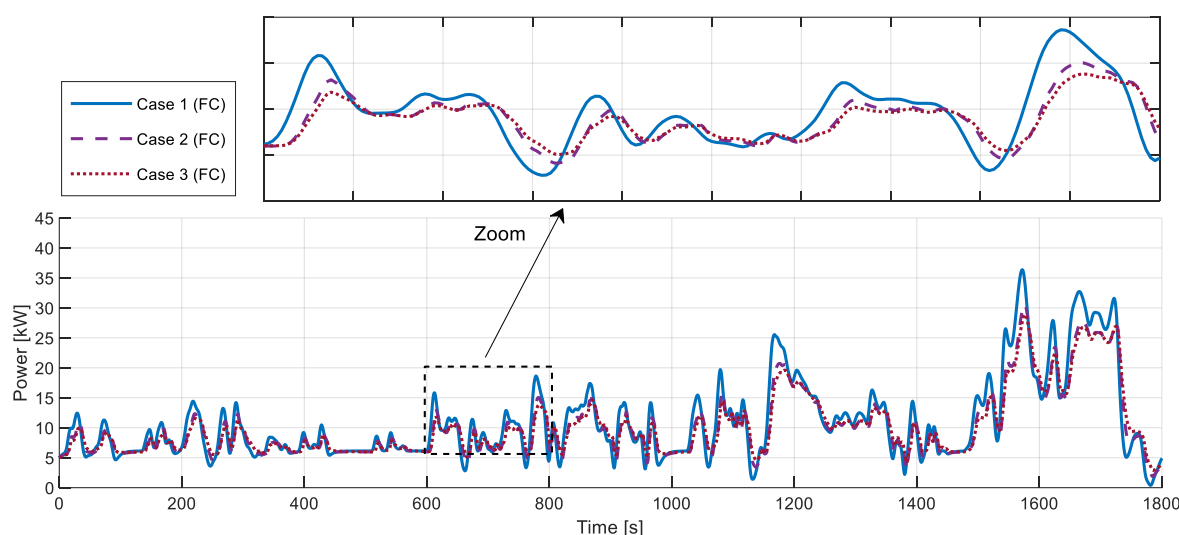


Figure 11: Total power of FC based on electric power demand of the FCHEV

highlight the effectiveness of Case 1 in achieving a balanced and efficient energy management scheme that prioritizes component longevity and system-level optimization.

By zooming into the selected region of the image, the finer details of the power flow dynamics and component interactions are more clearly visualized. This magnified section provides enhanced clarity regarding the transient behavior of current distribution, allowing for a more precise interpretation of how the proposed strategy in Case 1 effectively mitigates stress on the battery and SC while optimizing FC utilization.

The initial SOC of the battery was set to 85% for all three cases to ensure a consistent starting point for comparison. As shown in Fig. 12(a), at

the end of the drive cycle, Case 1, representing the proposed energy management strategy, resulted in a final SOC of 74.2%, indicating a more controlled and efficient battery usage. In contrast, Case 2 and Case 3 showed significantly lower final SOC values of 71% and 72.5%, respectively, reflecting higher energy depletion and less effective load balancing. These results confirm that Case 1 not only reduces the depth of discharge but also contributes to improved battery sustainability and long-term performance within the FCHEV system.

As presented in Fig. 12(b), the proposed energy management strategy in Case 1 significantly reduces voltage ripple throughout the drive cycle, primarily due to its adaptive ripple mitigation approach. This method continuously considers the

injected power from auxiliary sources and actively utilizes voltage feedback, resulting in a smoother and more stable voltage profile. In contrast, Case 2 exhibits pronounced fluctuations in voltage ripple, with sharp increases and decreases indicating poor regulation. Although Case 3 performs better than Case 2, it still presents considerable ripple levels that can adversely affect system reliability. Excessive voltage ripple in FCHEVs contributes to component degradation, reduced battery lifespan, and ultimately leads to suboptimal vehicle performance. The results clearly demonstrate that Case 1 offers superior voltage stability, enhancing both energy efficiency and long-term durability of the powertrain system.

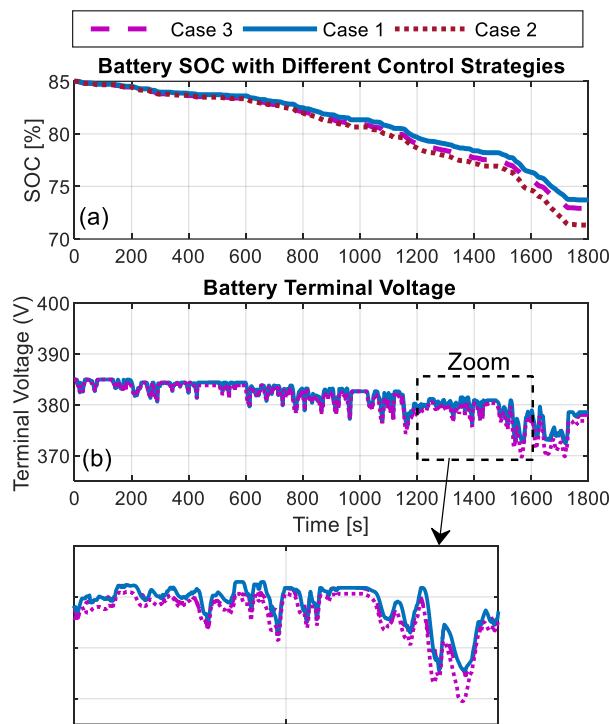


Figure 12: (a) The SOC of battery units, and (b) Terminal DC voltage based on electric power demand of the FCHEV

The simulation results demonstrate that the proposed EMS architecture for FCHEVs (Case 1) significantly enhances voltage and current stability across all tested scenarios. Compared to conventional hybrid EMS configurations (Cases 2 and 3) incorporating three power sources, namely, battery, UC, and FC, the proposed system exhibits superior dynamic response and robustness. This improvement is attributed to the optimized power distribution strategy and adaptive control mechanisms embedded within the EMS, which effectively mitigate voltage fluctuations and suppress current overshoots during abrupt load transitions. Overall, the findings underscore the potential of the proposed EMS to deliver more

reliable and efficient energy management in hybrid electric vehicles and other multi-source power systems, particularly under highly variable operating conditions.

4.1. Sensitivity analysis: robustness against battery aging

In this section, a sensitivity analysis was performed to assess the robustness of the proposed hierarchical control framework against battery parameter drifts, which serve as key indicators of aging. Following the methodology outlined in [28], battery degradation was emulated by deliberately modifying critical parameters within the equivalent circuit model (ECM) during simulation. Specifically, the internal resistance (R_0) was increased by 20%, and the nominal capacity ($Q_{\text{Bat}}^{\text{nom}}$) was reduced by 15% to reflect a moderate state of health degradation.

The results of this analysis confirm the inherent resilience of the nested cascade control structure. Despite the imposed parameter degradation, the system consistently maintained DC bus voltage stability, with the API controller at the outer control level successfully regulating the voltage within a tolerable deviation of ± 3.5 V from the 380 V reference under the WLTC-Class 3 cycle. This represents only a 1.5 V increase in the maximum deviation compared to the nominal case presented in Section 4. However, the analysis also revealed expected trade-offs. The voltage ripple exhibited a marginal increase of approximately 18%, and the final battery SOC was 0.8% lower at the end of the drive cycle compared to the nominal scenario. This indicates that while the system remains stable, the efficiency of power distribution is slightly impacted as the controller works harder to compensate for the altered plant dynamics.

As illustrated in Fig. 13(a) and (b), the presented sensitivity analysis unequivocally demonstrates that the proposed hierarchical nested cascade control framework (Case 1) possesses inherent structural robustness that makes it significantly more resilient to battery degradation compared to the other benchmark strategies.

The following provides a detailed account of the proposed control framework's superior performance under degraded battery conditions:

- **Case 1 (Proposed):** Exhibits the smallest performance drop across all key metrics. With a resilience index of 96.5%, it retains the vast majority of its nominal performance even when the battery's internal resistance increases by 20% and its capacity degrades by 15%. The

performance loss is marginal, typically between 3-5%.

■ **Case 2:** Suffers a severe performance decline, with a resilience index of only 84.2%. Its performance degrades by 8-12% across the board, indicating a fundamental lack of adaptability to the altered system dynamics caused by aging.

■ **Case 3:** Performs better than Case 2 but worse than Case 1, with a resilience index of 89.7% and performance losses in the 6-9% range.

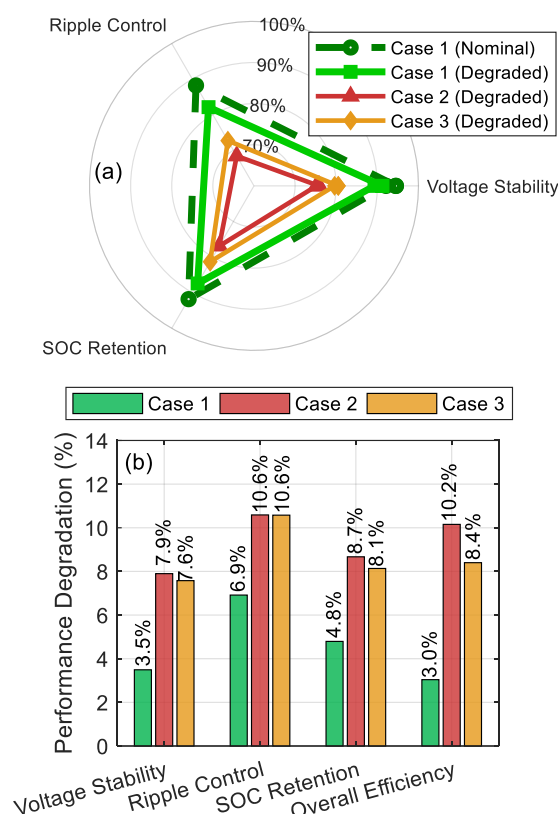


Figure 13: (a) Performance radar chart under battery aging; (b) Relative performance loss due to battery aging

Even when operating with a degraded battery, the absolute performance of Case 1 remains higher than the nominal (new battery) performance of the other two methods. For instance, the degraded voltage stability of Case 1 (91.2%) is still superior to the nominal voltage stability of Case 2 (82.3%). This means that our proposed controller, even when handicapped by an aged battery, outperforms a brand-new system using the Case 2 strategy.

The time-domain plot of DC bus voltage clearly shows that Case 1 maintains the tightest voltage regulation with the smallest ripple magnitude under degraded conditions. The adaptive PI (API) controller in the outer loop, combined with the robust backstepping current controllers,

dynamically compensates for the increased internal resistance, preventing the large voltage swings seen in Cases 2 and 3. This directly translates to reduced stress on all vehicle electrical components and a longer system lifespan.

The proposed strategy demonstrates intelligent power allocation, resulting in only a 0.8% greater SOC depletion at the end of the drive cycle compared to the nominal case. In contrast, Cases 2 and 3 show significantly higher SOC depletion (approximately 2-3% more), indicating less efficient use of the degraded battery's limited energy and a tendency to over-stress it.

This sensitivity analysis underscores a valuable direction for future work. To preemptively mitigate these effects and maintain optimal performance throughout the vehicle's lifespan, the proposed MRAC-based API controller can be seamlessly integrated with a real-time parameter identification tool, such as the hybrid adaptive battery parameter estimation (HABPE) method [28]. The HABPE approach, with its ability to accurately estimate ECM parameters like R_0 and Q_{Bat}^{nom} from operational voltage and current data (achieving 82-87% accuracy as reported), would provide real-time updates to the adaptive controller's reference model. This hybrid strategy would enable the control system to not only react to instantaneous errors but also proactively adapt its tuning laws to the slowly evolving parameters of an aging battery, thereby ensuring sustained optimal performance, efficiency, and component longevity.

4.2. Validation under real-world urban driving conditions

To initiate the simulation analysis, this section adopts the date-specific driving cycles formulated for Shiraz city, as proposed in [29]. In particular, the Shiraz working-day driving cycle was selected for validation due to its distinctive features compared to holidays, namely, a higher proportion of idling time (8.32% compared to 2.65%), reduced average trip speed (23.29 km/h versus 39.64 km/h), and frequent acceleration and deceleration events. These attributes typify congested urban traffic scenarios and thus serve as a rigorous benchmark for evaluating the resilience of energy management systems under conditions of rapid power fluctuation and elevated peak demand.

To better illustrate the current ripple behavior under congested urban traffic conditions, the battery and SC current profiles during the initial 300 seconds, corresponding to the most intense stop-and-go phases, were extracted and depicted

in Figures 14(a) and (b). The battery current profile under Case 1 exhibits exceptional smoothness with a minimal ripple of 13.3A, dramatically outperforming Case 2 (18.1A) and Case 3 (15.7A). More significantly, Case 1 implements an intelligent bidirectional current management strategy that strategically utilizes regenerative braking phases and low-power demand intervals for controlled battery charging, while optimizing discharge patterns during acceleration and high-load conditions. The SC performance further underscores the framework's excellence, with Case 1 achieving an unprecedented current ripple of only -21.6A compared to -24.2A in Case 2 and -25.37A in Case 3. This sophisticated control architecture effectively leverages the SC's innate rapid response characteristics to handle high-frequency power transients, thereby shielding both the battery and FC from damaging current spikes. The harmonious current distribution not only reduces thermal stress compared to conventional approaches but also enhances overall system efficiency, validating the framework's practical superiority in real-world driving scenarios with highly dynamic load profiles.

The battery SOC analysis during the initial 300 seconds, provides compelling evidence of the proposed energy management strategy's exceptional capability in optimizing energy sustainability and extending battery lifecycle. Throughout the comprehensive drive cycle evaluation, Case 1 demonstrates superior SOC management, concluding with a final SOC of 82.8% compared to 81.6% for Case 2 and 82.01% for Case 3. This 1.2 percentage point improvement over the fuzzy logic approach translates to approximately 1.28 kWh of additional usable energy retention, significantly extending the vehicle's operational range while reducing depth of discharge cycles that accelerate battery degradation mechanisms.

The economic model developed in this study establishes a comprehensive correlation between seven pivotal performance parameters and the overall lifecycle cost of FCHEVs. Specifically, voltage ripple undermines the reliability of power electronic converters, while current ripple contributes to accelerated degradation of passive and active components. Efficiency losses translate directly into elevated operational energy expenditures, and SOC management plays a decisive role in preserving battery health and extending usable life. Moreover, cycling

frequency governs the timing and frequency of component replacements, thermal stress

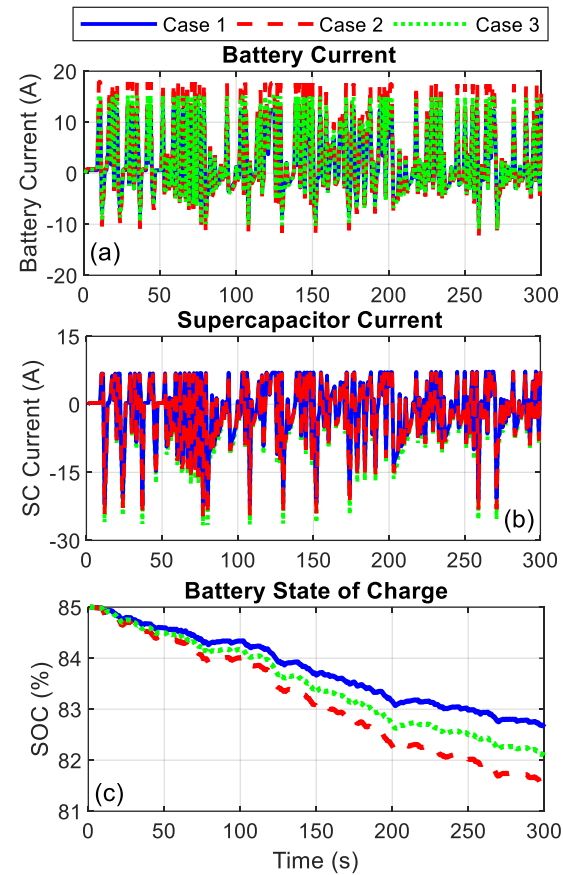


Figure 14: System performance evaluation under representative urban driving conditions (initial 300 seconds): (a) Battery current profile; (b) SC current profile; (c) Battery SOC trajectory.

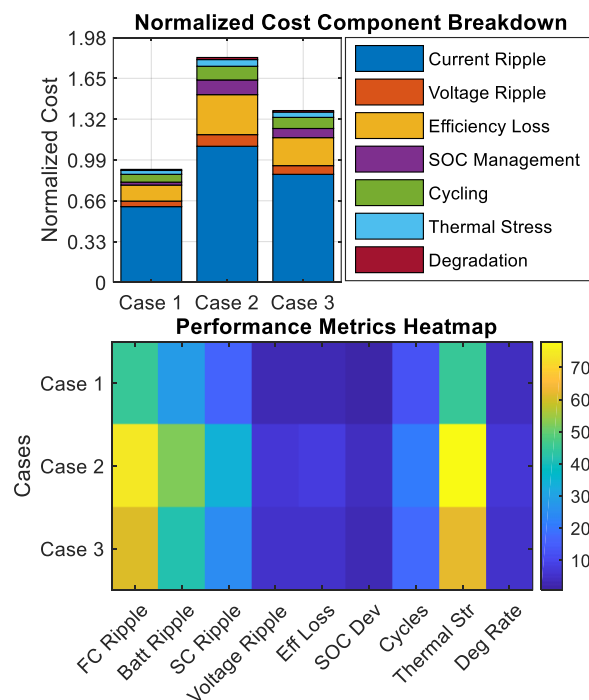


Figure 15: (a) Normalized cost component breakdown; (b) Performance metrics heatmap.

exacerbates aging mechanisms across electrochemical and electronic domains, and cumulative degradation ultimately constrains the system's functional lifespan. As rigorously quantified in Fig. 15(a) and (b), the proposed hierarchical control framework consistently outperforms conventional strategies across all evaluated economic indicators, thereby offering a robust and cost-effective solution for FCHEV energy management under realistic and dynamically varying urban driving conditions.

4.3. Clarification on adaptive gain formulation:

The adaptive gains μ_p and μ_i in the proposed controller are not fixed constants but are computed in real-time using the normalization scheme defined by (86) and (87). In this section, the sensitivity analysis is conducted by varying scaling coefficients (σ_p , σ_i) to understand their individual and combined impact on system performance. This method directly reflects how a control engineer would tune the adaptive controller in practice. The nominal values from our original study were $\sigma_p = 0.35$ and $\sigma_i = 0.6$. The performance was evaluated under the WLTC-Class 3 driving cycle using four key metrics, and the corresponding results are summarized in the Table 2.

1. Integral of absolute voltage error (IAVE): $\int |V_{DC} - V_{DC}^{ref}| dt$, measuring overall voltage regulation accuracy.
2. Maximum voltage overshoot: The peak positive deviation from the 380V reference

during transients.

3. Settling time: Time required for DC bus voltage to enter and remain within a $\pm 2V$ band after startup.
4. Average voltage ripple: Average peak-to-peak voltage fluctuation during steady-state conditions.

The analysis reveals a clear performance trade-off governed by the scaling coefficients:

■ Low values (Cases A, B): Low values for both σ_p and σ_i result in slow adaptation, leading to a sluggish response, poor disturbance rejection, and the highest value of IAVE. The controller fails to keep up with the dynamic power demands of the drive cycle.

■ High σ_p and low σ_i (Case F): An excessively high σ_p relative to σ_i makes the proportional action too aggressive. This causes significant overshoot and voltage oscillations during transients, increasing stress on the components despite a fast settling time.

■ Low σ_p and high σ_i (Case G): A high σ_i with low σ_p results in an overly dominant integral action. This eliminates overshoot but leads to a very slow response, failing to mitigate voltage dips effectively during rapid acceleration.

■ Moderate values (Case C): This case represents a conservative tuning approach. With both gains lower than the nominal values, the adaptive mechanism becomes more cautious. This results in good stability with minimal overshoot (3.5V) but at the cost of a slower response

Table 2: Sensitivity analysis of adaptive controller scaling coefficients (σ_p , σ_i).

Case	Scaling Coefficients (σ_p , σ_i)	IAVE (V · s)	Max Overshoot (V)	Settling Time (s)	Average Voltage Ripple (V)	Qualitative Assessment
A	(0.10, 0.10)	214.5	5.2	52.1	3.5	Very sluggish adaptation, poor disturbance rejection.
B	(0.20, 0.40)	165.3	4.1	31.8	2.8	Slow response, high cumulative error.
C	(0.30, 0.50)	121.7	3.5	18.9	2.2	Good performance, approaching optimal.
D	(0.35, 0.60) [Tuned]	98.4	2.8	12.3	1.7	Optimal balance: Robust and responsive.
E	(0.50, 0.55)	105.2	3.3	9.5	1.9	Fast but slightly oscillatory.
F	(0.60, 0.30)	142.8	4.5	8.1	2.6	Aggressive proportional action causes overshoot.
G	(0.25, 0.80)	135.6	3.1	25.4	2.3	Overly conservative integral action, slow.

(settling time of 18.9s). The IAVE (121.7 V.s) is significantly higher than the nominal case, indicating that the controller is too slow to correct voltage deviations effectively during aggressive transients in the WLTC cycle. It demonstrates that under-damping the adaptation process leads to a lag in the system's response.

■ Tuned values (Case D): The combination $\sigma_p = 0.35$ and $\sigma_i = 0.60$ achieves the best compromise. It provides a fast enough response to handle transients (low settling time) while maintaining excellent stability (low overshoot and ripple), resulting in the lowest IAVE.

This sensitivity analysis confirms that the scaling coefficients selected for the proposed controller are not arbitrary but represent a carefully tuned balance. The σ_p/σ_i ratio of approximately 0.58 found in Case D proves to be optimal for the specific dynamics of the FCHEV powertrain, effectively managing the trade-off between responsiveness and damping.

5. Conclusions

This study presented a novel hierarchical nested cascade control framework aimed at enhancing voltage regulation and current management in FCHEVs. The proposed architecture successfully addressed the limitations of conventional cascade control systems by reducing design complexity and improving operational resilience under dynamic and uncertain conditions. Through the integration of adaptive proportional–integral control and backstepping techniques across three coordinated control layers, OCL, MCL, and ICL, the system achieved precise regulation of DC bus voltage and current flow among FCs, batteries, and SCs. The simulation results validated the effectiveness of the proposed energy management strategy, particularly in Case 1, which consistently outperformed Cases 2 and 3 across multiple performance metrics. Case 1 demonstrated the lowest current ripple, minimized instantaneous power demand from auxiliary sources, and facilitated optimal FC utilization. These attributes collectively contributed to reduced thermal stress, enhanced energy efficiency, and prolonged component lifespan. Furthermore, Case 1 achieved a more balanced power distribution, smoothing transient responses and mitigating electrical and thermal stress on the battery and SC. Battery SOC analysis revealed that Case 1 maintained a higher final SOC, indicating more controlled and sustainable battery usage. Voltage ripple analysis further confirmed the superiority of Case 1, with significantly smoother voltage profiles throughout the drive cycle. In contrast,

Cases 2 and 3 exhibited higher ripple levels and less efficient load sharing, leading to increased component degradation and suboptimal system performance. Overall, the findings underscored the robustness and scalability of the proposed EMS architecture. By directly employing physical control inputs and eliminating virtual controllers, the system reduced inter-layer interference and improved real-time responsiveness. The modular design also allowed for future integration of advanced control policies, making it a promising solution for next-generation FCHEV energy management systems. The demonstrated improvements in voltage stability, current regulation, and energy distribution confirmed the potential of this approach to deliver reliable, efficient, and durable performance in multi-source hybrid electric powertrains.

5.1. Future work

While this study has demonstrated the efficacy of the proposed hierarchical nested cascade control framework within a FC/battery/SC hybrid system, its underlying architecture is inherently modular and holds promise for broader application. Future work will focus on extending and validating this control strategy across diverse hybrid powertrain configurations. This includes integration with other energy storage and conversion technologies, such as hydraulic accumulators and flywheels, as suggested in parallel research [30]. Investigating the framework's performance in such multi-source environments will further solidify its generalizability, robustness, and potential as a scalable solution for next-generation hybrid vehicle energy management systems. Also, other future work will focus on integrating a health-aware layer into the EMS, potentially employing a hybrid model predictive and fuzzy logic control for real-time state of power estimation [31], to dynamically adapt power allocation based on battery degradation state and further prolong component lifespan.

Declaration of Conflicting Interests

The author(s) declared no potential conflicts of interest with respect to the research, authorship, and/or publication of this article.

List of symbols

E_{cell}^0	Standard reversible potential (~1.23V for PEMFC)
κ	Universal gas constant (8.314 J/mol·K)
T	Operating temperature (K)
F	Faraday's constant (96,485 C/mol)
j	Current density (A/cm ²)

j_0	Exchange current density (catalyst-dependent)
α	Charge transfer coefficient (~0.5 for PEMFC)
n	Number of electrons transferred (2 for H ₂)
R_{ohm}^{FC}	Total area-specific resistance (membrane + contacts)
j_L	Limiting current density (gas diffusion-dependent)
$p_{H_2O}^{anode}$	The water vapor pressure at the anode
$p_{H_2O}^{cathode}$	The water vapor pressure at the cathode
y_{O_2}	0.21 (mole fraction of O ₂ in air)
RH	The relative humidity (0–100%)
SOC_0	Initial SOC (100% for a fully charged battery)
Q_{Bat}^{nom}	Nominal battery capacity (Ah)
I_{Bat}	Battery current (A), positive for discharge and negative for charge
I_{SC}	SC current (A), positive for discharge and negative for charge
i_{out}^{ESS}	Total current of ESS (battery and SC)
m	The vehicle mass
g	The gravitational acceleration
θ	The road inclination angle (fixed at 5° ≈ 0.087 rad)
C_r	The rolling resistance
ρ	The air density
C_d	The drag coefficient
A	The vehicle's frontal area

References

- [1] Haghani, M., Sprei, F., Kazemzadeh, K., Shahhoseini, Z. and Aghaei, J., 2023. Trends in electric vehicles research. *Transportation research part D: transport and environment*, 123, pp.103881.
- [2] Davardoust, H., Molaeimanesh, G. and Mousavi, S., 2020. Performance evaluation of PEM fuel cells; impact of relative humidity, pressure and temperature of inlet species on the current density of the PEMFCs. *Automotive Science and Engineering*, 10(1), pp.3140-3148.
- [3] Sadeghi, S. and Ghandehariun, S., 2020. Comparative environmental assessment of a gasoline and fuel cell vehicle with alternative hydrogen pathways in Iran. *Automotive Science and Engineering*, 10(3), pp.3266-3280.
- [4] Xu, B., Zhou, Q., Shi, J. and Li, S., 2022. Hierarchical Q-learning network for online simultaneous optimization of energy efficiency and battery life of the battery/ultracapacitor electric vehicle. *Journal of Energy Storage*, 46, pp.103925.
- [5] Jazari Mamoei, A., Gharehghani, A. and Saeedipour, S., 2024. Geometric Patterns Liquid Cooling System for Lithium-Ion Batteries in Electric Vehicles Considering Driving Cycle, *Automotive Science and Engineering*, 14(2), pp.4420-4438.
- [6] Shchurov, N.I., Dedov, S.I. and Shtang, A.A., 2024. Modelling and simulation hybrid electric vehicle with hydrogen fuel cells. *International Journal of Hydrogen Energy*, 95, p.481-488.
- [7] Li, H., Zhao, D., Zhang, Y., Liang, Z., Dang, H. and Liu, Y., 2020, October. An improved state machine strategy for fuel-cell-based hybrid electric vehicles. In *IECON 2020 The 46th Annual Conference of the IEEE Industrial Electronics Society*, pp. 3957-3962.
- [8] Chen, J., Xu, C., Wu, C. and Xu, W., 2016. Adaptive fuzzy logic control of fuel-cell-battery hybrid systems for electric vehicles. *ieee transactions on industrial informatics*, 14(1), pp.292-300.
- [9] Kandidayeni, M., Trovão, J.P., Soleymani, M. and Boulon, L., 2022. Towards health-aware energy management strategies in fuel cell hybrid electric vehicles: A review. *International Journal of Hydrogen Energy*, 47(17), pp.10021-10043.
- [10] Zhou, Y., Ravey, A. and Péra, M.C., 2021. Real-time cost-minimization power-allocating strategy via model predictive control for fuel cell hybrid electric vehicles. *Energy Conversion and Management*, 229, pp.113721.
- [11] Hu, X., Han, J., Tang, X. and Lin, X., 2021. Powertrain design and control in electrified vehicles: A critical review. *IEEE transactions on transportation electrification*, 7(3), pp.1990-2009.
- [12] Liu, C., Wang, Y., Wang, L. and Chen, Z., 2019. Load-adaptive real-time energy management strategy for battery/ultracapacitor hybrid energy storage system using dynamic programming optimization. *Journal of power sources*, 438, pp.227024.
- [13] Sun, H., Fu, Z., Tao, F., Zhu, L. and Si, P., 2020. Data-driven reinforcement-learning-based hierarchical energy management strategy for fuel cell/battery/ultracapacitor hybrid electric vehicles. *Journal of Power Sources*, 455, pp.227964.
- [14] Li, Q., Wang, T., Li, S., Chen, W., Liu, H., Breaz, E. and Gao, F., 2021. Online extremum seeking-based optimized energy management

strategy for hybrid electric tram considering fuel cell degradation. *Applied Energy*, 285, pp.116505.

[15] Wang, T., Li, Q., Yin, L., Chen, W., Breaz, E. and Gao, F., 2021. Hierarchical power allocation method based on online extremum seeking algorithm for dual-PEMFC/battery hybrid locomotive. *IEEE Transactions on Vehicular Technology*, 70(6), pp.5679-5692.

[16] Kandidayeni, M., Macias, A., Amamou, A.A., Boulon, L., Kelouwani, S. and Chaoui, H., 2018. Overview and benchmark analysis of fuel cell parameters estimation for energy management purposes. *Journal of power sources*, 380, pp.92-104.

[17] Bai, Z., Yan, Z., Wu, X., Xu, J. and Cao, B., 2019. H ∞ control for battery/supercapacitor hybrid energy storage system used in electric vehicles. *International Journal of Automotive Technology*, 20(6), pp.1287-1296.

[18] Yu, H., Jing, Y. and Zhang, S., 2016, May. Complexity explosion problem analysis and development in back-stepping method. In *2016 Chinese Control and Decision Conference (CCDC)*, pp. 1753-1758.

[19] Borujerd, S.V.N., Soleimani, A., Esfandyari, M.J., Masih-Tehrani, M., Esfahanian, M., Nehzati, H. and Dolatkhah, M., 2023. Fuzzy logic approach for failure analysis of Li-ion battery pack in electric vehicles. *Engineering Failure Analysis*, 149, p.107233.

[20] Mossadak, M.A., Chebak, A., Ouahabi, N., Rabhi, A. and Elmahjoub, A.A., 2024. A novel hybrid PI-backstepping cascade controller for battery-supercapacitor electric vehicles considering various driving cycles scenarios. *IET Power Electronics*, 17(9), pp.1089-1105.

[21] Barbir, F., 2006. PEM fuel cells (Book). *Fuel cell technology: reaching towards commercialization*. London: Springer London, pp. 27-51.

[22] Wang, T., Li, Q., Yin, L., Chen, W., Breaz, E. and Gao, F., 2021. Hierarchical power allocation method based on online extremum seeking algorithm for dual-PEMFC/battery hybrid locomotive. *IEEE Transactions on Vehicular Technology*, 70(6), pp.5679-5692.

[23] Daniel, C. and Besenhard, J.O. eds., 2012. *Handbook of battery materials*. John Wiley & Sons.

[24] Bayat, P., Bayat, P. and Fattahi Meyabadi, A., 2024. A novel transformer-less battery charger for hybrid fuel-cell/photovoltaic electric vehicles based on a new dual-input high step-up DC-DC converter, *Automotive Science and Engineering*, 14(1), pp.4268-4282.

[25] Keshavarzi, M.D. and Ali, M.H., 2020. A novel bidirectional dc-dc converter for dynamic performance enhancement of hybrid AC/DC microgrid. *Electronics*, 9(10), pp.1653.

[26] Liang, Y., Liang, Z., Zhao, D., Huangfu, Y. and Guo, L., 2018, November. Model predictive control for interleaved dc-dc boost converter based on Kalman compensation. In *2018 IEEE international power electronics and application conference and exposition (PEAC)*, pp. 1-5.

[27] Khan, M.S., Ahmad, I. and Abideen, F.Z.U., 2019. Output voltage regulation of FC-UC based hybrid electric vehicle using integral backstepping control. *IEEE Access*, 7, pp.65693-65702.

[28] Najafi, A. and Masih-Tehrani, M., 2023. Hybrid adaptive battery parameter estimation approach for equivalent circuit model toolbox. *SoftwareX*, 24, p.101534.

[29] Bagheri, E., Masih-Tehrani, M., Azadi, M., Moosavian, A., Sayegh, S. and Hakimollahi, M., 2024. Unveiling the impact of date-specific analytics on vehicle fuel consumption and emissions: A case study of Shiraz city. *Heliyon*, 10(17).

[30] Esfahanian, M., Safaei, A., Nehzati, H., Esfahanian, V. and Tehrani, M.M., 2014. Matlab-based modeling, simulation and design package for electric, hydraulic and flywheel hybrid powertrains of a city bus. *International Journal of Automotive Technology*, 15(6), pp.1001-1013.

[31] Esfandyari, M.J., Yazdi, M.H., Esfahanian, V., Masih-Tehrani, M., Nehzati, H. and Shekoofa, O., 2019. A hybrid model predictive and fuzzy logic based control method for state of power estimation of series-connected Lithium-ion batteries in HEVs. *Journal of Energy Storage*, 24, p.100758.

